



## Article

# Facile and Green Synthesis of Highly Fluorescent Carbon Quantum Dots from Water Hyacinth for the Detection of Ferric Iron and Cellular Imaging

Pei Zhao <sup>1</sup>, Qin Zhang <sup>1,2,\*</sup> , Juanjuan Cao <sup>1</sup>, Cheng Qian <sup>1</sup>, Jing Ye <sup>1</sup>, Siyuan Xu <sup>1</sup>, Yonggui Zhang <sup>1</sup> and Yanbin Li <sup>1,2,\*</sup>

<sup>1</sup> College of Biological and Food Engineering, Anhui Polytechnic University, Wuhu 241000, China; lvxmzp@163.com (P.Z.); cjj18890973009@163.com (J.C.); qiancheng9981@163.com (C.Q.); a2235672022@163.com (J.Y.); shanyazi0605@163.com (S.X.); xjagcdzyg@163.com (Y.Z.)

<sup>2</sup> Anhui Engineering Laboratory for Industrial Microbiology Molecular Breeding, College of Biological and Food Engineering, Anhui Polytechnic University, Wuhu 241000, China

\* Correspondence: jhtabszq@163.com (Q.Z.); lyb@ahpu.edu.cn (Y.L.)

**Abstract:** Natural biomass is used for facile synthesis of carbon quantum dots (CQDs) with high fluorescence, owing to its abundance, low cost, and eco-friendliness. In this study, a bottom-up hydrothermal method was used to prepare CQDs from water hyacinth (wh) at a constant temperature of 180 °C for 12 h. The synthesized wh-CQDs had uniform size, amorphous graphite structure, high water solubility (containing multiple hydroxyl and carboxyl groups on the surface), excitation light-dependent characteristics, and high photostability. The results showed that the aqueous solution of CQDs could detect Fe<sup>3+</sup> rapidly, sensitively, and highly selectively with a detection limit of 0.084 μM in the linear range of 0–330 μM, which is much lower than the detection limit of 0.77 μM specified by the World Health Organization. More importantly, because the wh-CQDs were synthesized without any additives, they exhibited low toxicity to *Klebsiella* sp. cells even at high concentrations. Moreover, wh-CQDs emitted bright blue fluorescence in *Klebsiella* sp. cells, indicating its strong penetrating ability. Correspondingly, the fluorescent cell sorting results also revealed that the proportion of cell internalization reached 41.78%. In this study, wh-CQDs derived from natural biomass were used as high-performance fluorescent probes for Fe<sup>3+</sup> detection and *Klebsiella* sp. imaging. This study is expected to have great significance for the application of biomass carbon spots in the field of cellular imaging and biology.

**Keywords:** water hyacinth; green synthesis; carbon quantum dots; Fe<sup>3+</sup> sensing; fluorescent probe; cellular imaging



**Citation:** Zhao, P.; Zhang, Q.; Cao, J.; Qian, C.; Ye, J.; Xu, S.; Zhang, Y.; Li, Y. Facile and Green Synthesis of Highly Fluorescent Carbon Quantum Dots from Water Hyacinth for the Detection of Ferric Iron and Cellular Imaging. *Nanomaterials* **2022**, *12*, 1528. <https://doi.org/10.3390/nano12091528>

Academic Editor: Hideya Kawasaki

Received: 5 April 2022

Accepted: 29 April 2022

Published: 1 May 2022

**Publisher's Note:** MDPI stays neutral with regard to jurisdictional claims in published maps and institutional affiliations.



**Copyright:** © 2022 by the authors. Licensee MDPI, Basel, Switzerland. This article is an open access article distributed under the terms and conditions of the Creative Commons Attribution (CC BY) license (<https://creativecommons.org/licenses/by/4.0/>).

## 1. Introduction

Biomass materials are a crucial renewable source of carbon on earth. Based on differences in structure, composition, and molecular weight, raw materials for synthetic biomass can be divided into three categories: micro-molecules derived from biomass (e.g., citric acid, glucose, etc.), biomass components (e.g., cellulose, hemicellulose, lignin, etc.), and natural biomass (e.g., straw, crab shells, etc.) [1,2]. Approximately 181 billion tons of biomass waste is annually produced and not treated effectively worldwide [3]. This not only burdens the ecology but also is a waste of a significant amount of resources. Currently, many researchers use forest by-products, agricultural residues, food waste, and industrial residues, such as lignin, chitosan, rice husk, cherry stone powder, waste tar, as green raw materials for synthetic carbon nanoparticles [4–8]. The effective conversion of biomass waste into carbon nanoparticles could reduce the harm of organic waste to the environment through resource management and alleviate the pressure of resource shortage.

Quantum dots are semiconductor nanoparticles, and traditional fluorescent quantum dots are semiconductor quantum dots (SQDs), which emit light at a specific frequency under a certain electric field or optical pressure and are used in the fields of sensing [9], drug carriers [10], and biological imaging [11]. However, the applications of SQDs in analytical detection and biological imaging are limited because they contain heavy metal ions and are highly toxic. Carbon quantum dots (CQDs) are a member of the carbon nanomaterial family; they are generally smaller than 10 nm and are mainly composed of C and O [12]. CQDs have better biocompatibility, low toxicity, water solubility, and photoluminescence characteristics than SQDs and can be applied in the fields of bioimaging, drug carriers, gene delivery, metal ion detection, sensing and nanothermometer [13–18]. The synthesis methods of CQDs include top-down and bottom-up methods: cracking of different carbon source materials and carbonization of small molecules or polymers [19]. Among them, the hydrothermal method, a bottom-up approach possessing the advantages of energy efficiency, low cost, and convenient operation, is mainly used to carbonize organic matter to form luminescent CQDs at high temperatures and pressures. Trace elements and heteroatoms present in the biomass accumulate on the surface to form abundant functional groups, which are good precursors for the formation of CQDs [20]. Biomass, such as saponins, coconut husk, avocados, corncobs, kiwifruit, passion fruit peel, and corn stalks, can be used as carbon precursors in the green synthesis of CQDs and show great potential for CQDs production [21–27]. Moreover, biomass CQDs possess advantages in the field of bioimaging because of their excellent fluorescence properties and low cytotoxicity. Chan et al. reviewed the synthesis of CQDs from various natural biomass [28]. However, the current objects of biomass CQD imaging studies are primarily cancer cells and seldom bacterial cells (e.g., cells of *Escherichia coli* and *Staphylococcus aureus*) [29–32]. To the best of our knowledge, imaging and toxicity studies of biomass CQDs on the hydrogen-producing bacterium *Klebsiella* sp. have rarely been reported. Therefore, it is of vital importance to use biomass CQDs with low toxicity obtained via green synthesis to trace bacterial growth behaviors during hydrogen production.

Iron is one of the most important trace elements in biological systems and a common heavy metal pollutant in industrial wastewater and drinking water [33]. The detection of ferric iron is of great importance for biological systems, as it plays a crucial role in the biochemical pathways of living cells [34]. Excess or lack of  $\text{Fe}^{3+}$  ions may cause body disorders and various diseases, where excess  $\text{Fe}^{3+}$  ions can deteriorate the function of heart, pancreas, and lungs, and even lead to cancer, whereas a lack of  $\text{Fe}^{3+}$  leads to anemia [35]. Therefore, it is essential to develop a safe, efficient, sensitive, and selective method for detecting  $\text{Fe}^{3+}$ . Among many methods, the detection of  $\text{Fe}^{3+}$  by biomass-derived CQDs has the advantages of high sensitivity, low detection limit, simple operation, and fast response speed compared with spectrophotometry, colorimetry, and inductively coupled methods with complex operation and limited accuracy. For example, Chen et al. used lignin as a precursor to synthesize CQDs with a higher quantum yield (QY), wider detection range, and lower detection limit than some reported CQDs [36]. Therefore, excellent selectivity and sensitivity indicate that biomass CQDs are promising probes for detecting  $\text{Fe}^{3+}$ .

In this study, biomass CQDs with blue fluorescence properties were synthesized by hydrothermal green method using biomass water hyacinth (wh) as a carbon source, with a QY of 3.3%. Compared with the reported carbon dots derived from wh [37], the synthesis in the present study was greener, the particle size was more uniform, and the product could be more widely used in biological applications because no chemical reagents were added. The physicochemical properties of wh-CQDs, such as particle size, crystal structure, surface functional groups, elemental composition, and optical properties, were characterized using various techniques. The wh-CQDs were tested for  $\text{Fe}^{3+}$ , and their detection range for  $\text{Fe}^{3+}$  was 0–330  $\mu\text{M}$ ; simultaneously, their detection limit was 0.084  $\mu\text{M}$ , which is much lower than the detection limit specified internationally. Finally, the biocompatibility of the biomass-derived wh-CQDs was evaluated by cellular imaging, toxicity studies, and flow cytometry analysis on *Klebsiella* sp. The experiments revealed that our synthesized

wh-CQDs could be internalized into *Klebsiella* sp. and showed blue fluorescence, indicating good biocompatibility. The activity of *Klebsiella* sp. remained above 90% at 1000  $\mu\text{g}/\text{mL}$  of wh-CQDs. These results suggest that biomass wh-CQDs have good potential for biomedical applications.

## 2. Materials and Methods

### 2.1. Materials

Wh was collected locally, washed thrice with water, and air-dried. The samples were crushed to obtain a fine powder and sieved (Joyoung, Wuhu, China). Microporous membrane (0.22  $\mu\text{m}$ ), peptone, yeast extract, and agar were purchased from Sangon Biotech (Shanghai, China). Quinine sulfate (98%, suitable for fluorescence) and other chemical reagents, such as NaOH, NaCl, and the metal ion compounds, were of analytical reagent grade, supplied by Macklin Biotech (Shanghai, China), and used without further purification. Ultrapure water (HHitech, Shanghai, China) was used for all experiments.

### 2.2. Preparation of wh-CQDs

Synthesis of wh-CQDs: According to a published process, wh-CQDs were synthesized using a one-step hydrothermal method with some modifications (Figure 1) [37]. In this typical synthesis process, approximately 5 g of wh powder was dispersed in 50 mL of purified water under stirring, after which the mixture was transferred into a 100 mL Teflon-lined stainless-steel autoclave and heated at 180  $^{\circ}\text{C}$  for 12 h. After cooling to room temperature, the mixture was centrifuged at 8000 rpm for 20 min, and the supernatant was filtered using a 0.22  $\mu\text{m}$  microporous membrane to remove insoluble precipitate. The supernatant was then subjected to dialysis against purified water with a dialysis bag (molecular weight cutoff: 1 kDa) for 24 h to remove small molecules. The brown solution of wh-CQDs was stored at 4  $^{\circ}\text{C}$  for characterization and further use.

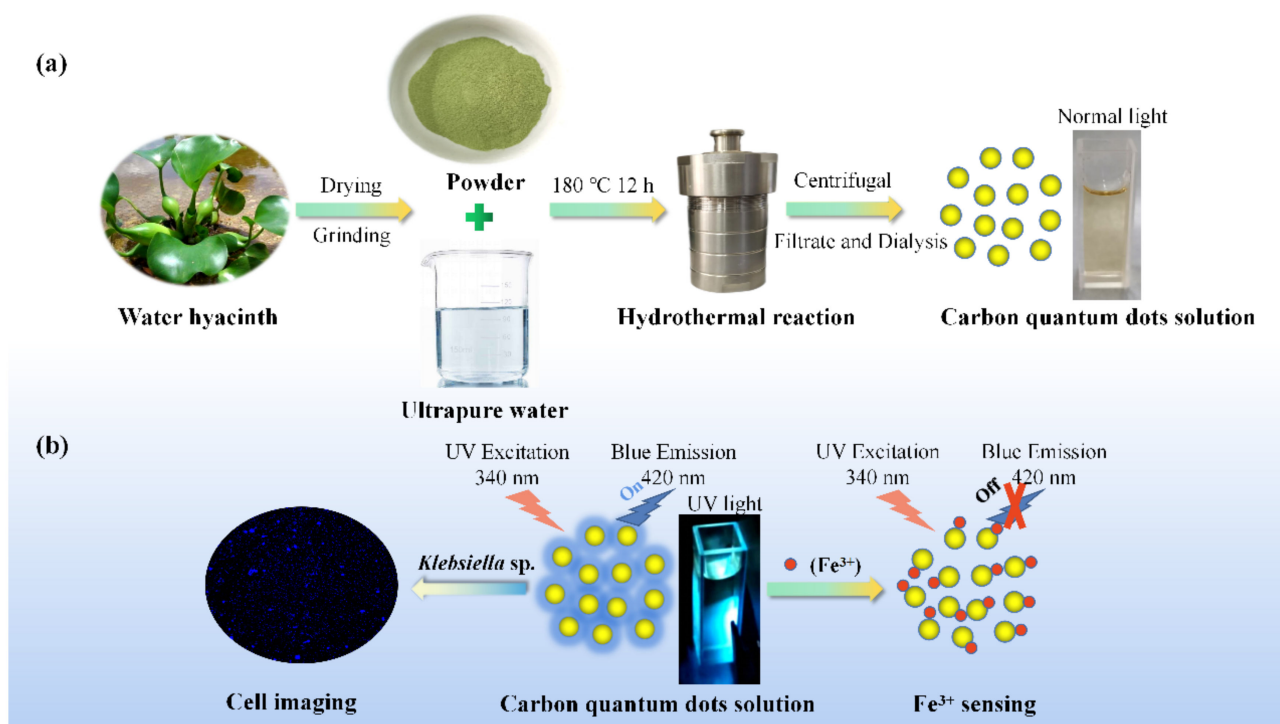


**Figure 1.** (a) Schematic of CQDs derived from wh and (b) their applications.

### 2.3. Characterizations

The surface morphology of the wh-CQDs was determined using a Tecnai G2 F30 S-TWIN field-emission transmission electron microscopy (TEM and HRTEM, FEI Corp.,

Portland, OR, USA) at an accelerating voltage of 200 kV. The particle size of the wh-CQDs was analyzed using image processing software Image J 1.52 and TEM micrographs, and the size distribution was calculated using Origin 8.0. Powder X-ray diffraction (XRD) analysis was conducted using a Bruker D8 Advance diffractometer (Bruker Corp., Billerica, MA, USA) with Cu K $\alpha$  radiation and a scanning scope of  $2\theta = 10\text{--}90^\circ$ . The functional group information of the wh-CQDs was analyzed using Fourier transform infrared spectroscopy (FTIR, Nicolet IS10, Nicolet Corp., Madison, WI, USA) in the range  $400\text{--}4000\text{ cm}^{-1}$ . For each measurement, the samples were scanned 64 times at a resolution of  $4\text{ cm}^{-1}$ . X-ray photoelectron spectroscopy (XPS) was used to characterize the content and robustness of various elements in the samples (Thermo, Waltham, MA, USA). Ultraviolet-visible (UV-Vis) absorption spectra were obtained using a Shimadzu 2550 UV-Vis spectrophotometer (Shimadzu, Tokyo, Japan). The two- and three-dimensional fluorescence spectra and fluorescence intensities of the wh-CQDs were recorded using an F-7100 fluorescence spectrometer (Hitachi, Tokyo, Japan) with the excitation and emission slits of 5 nm. Fluorescence lifetime measurements were performed on an FluoroMax-4 time-resolved fluorescence spectrophotometer (HORIBA, Kyoto, Japan).

#### 2.4. QY Calculations

QY calculations were performed using an established method. Quinine sulfate solution ( $\Phi = 54\%$  at 360 nm excitation light,  $\eta = 1.33$ ) was used as a standard reference to calculate the relative QY of the wh-CQDs. The specific operation steps were as follows: five different concentrations of wh-CQDs dispersions in water and quinine sulfate solutions in 0.1 M H<sub>2</sub>SO<sub>4</sub> were prepared. The absorbance of both wh-CQDs and quinine sulfate solution was adjusted to below 0.1 to reduce the internal filtration effect. The QY of wh-CQDs was calculated using the following Equation (1) [38]:

$$\Phi_S = \Phi_R \left( \frac{\text{Grad}_S}{\text{Grad}_R} \right) \left( \frac{\eta_S^2}{\eta_R^2} \right) \quad (1)$$

where Grad<sub>S</sub> and Grad<sub>R</sub> are the slopes of the integrated areas of the fluorescence intensity, and absorbance for wh-CQDs and quinine sulfate, respectively, and  $\eta$  is the refractive index of the solvent; subscripts S and R correspond to the wh-CQDs and quinine sulfate, respectively.

#### 2.5. Stability of wh-CQDs

The effects of pH (2–12), salt ion concentration (0.02, 0.04, 0.06, 0.08, and 0.1 M), and UV irradiation time (0, 10, 20, 30, 40, 50, and 60 min) on the fluorescence intensity of wh-CQDs were assessed. The fluorescence intensity was recorded using a spectrofluorometer at an excitation wavelength of 340 nm.

#### 2.6. Sensitivity and Selective Detection of Fe<sup>3+</sup> Ions

For the sensitivity experiment, ferric chloride hexahydrate (FeCl<sub>3</sub>) was dissolved in ultrapure water to prepare solutions with different Fe<sup>3+</sup> concentrations. A 300  $\mu\text{L}$  solution of wh-CQDs (1 mg/mL) was diluted 10-fold with ultrapure water to detect Fe<sup>3+</sup>; 3 mL of wh-CQDs (100  $\mu\text{g}/\text{mL}$ ) was mixed with 100  $\mu\text{L}$  of Fe<sup>3+</sup> solutions of different concentrations, and the mixtures were maintained for 3 min at room temperature. Fluorescence intensity was recorded using a spectrofluorometer at 340 nm with excitation and emission slits of 5 nm at a PMT voltage of 600 V.

To compare the sensitivity of the wh-CQDs toward different ions, the fluorescence spectra of different metal ions (Fe<sup>2+</sup>, Mg<sup>2+</sup>, NH<sub>4</sub><sup>+</sup>, Ni<sup>2+</sup>, Zn<sup>2+</sup>, K<sup>+</sup>, Na<sup>+</sup>, Mn<sup>2+</sup>, Co<sup>2+</sup>, Ba<sup>2+</sup>, Al<sup>3+</sup>, Ca<sup>2+</sup>, and Cu<sup>2+</sup>, 10 mM) with CQDs were obtained according to the steps described above.

### 2.7. Cell Viability Assay

The viability of *Klebsiella* sp. was determined using 96-well plates. First,  $10^5$  colony-forming units (CFUs) of cells were obtained by gradient dilution of optical density (OD). Then, 100  $\mu\text{L}$  of  $10^5$  CFU of bacterial cells was mixed with 100  $\mu\text{L}$  of wh-CQDs of different concentrations (31.25, 62.5, 125, 250, 500, 1000, and 2000  $\mu\text{g}/\text{mL}$ ) prepared in phosphate-buffered saline (PBS); bacterial culture without wh-CQDs was used as a control. After incubation at 37 °C for 24 and 48 h, the absorbance was recorded at a wavelength of 600 nm. Cell viability was calculated using Equation (2) [39]:

$$\text{Cell viability (\%)} = \frac{\text{OD}_{\text{treated}}}{\text{OD}_{\text{control}}} \times 100\% \quad (2)$$

where  $\text{OD}_{\text{control}}$  is the OD in the absence of wh-CQDs and  $\text{OD}_{\text{treated}}$  is the OD in the presence of wh-CQDs.

### 2.8. Cell Imaging

*Klebsiella* sp. were streaked on LB solid plates and cultured at 37 °C for 24 h. A single colony was inoculated in LB liquid medium, and an appropriate amount of synthetic CQD solution was added to the medium (150  $\mu\text{L}$  of 500  $\mu\text{g}/\text{mL}$  wh-CQDs in 2 mL medium). The mixture was incubated overnight at 37 °C under shaking at 200 rpm. The next day, 1 mL of culture medium was centrifuged and washed three times with PBS. Then, the bacterial cells were suspended in 500  $\mu\text{L}$  of PBS and kept at 4 °C for fluorescence imaging using Leica confocal microscope.

### 2.9. Flow Cytometry Analysis of Intracellular wh-CQDs

Flow cytometric analysis of *Klebsiella* sp. cells incubated with wh-CQDs was performed using a Beckman Coulter flow cytometer. Briefly, *Klebsiella* sp. bacterial cells were incubated with 500  $\mu\text{g}/\text{mL}$  wh-CQDs for 12 and 24 h at 37 °C to obtain  $10^5$  CFU/mL of bacteria by adjusting the OD value; 1 mL of the culture medium was centrifuged and washed three times with PBS, and then the bacterial cells were suspended in 500  $\mu\text{L}$  of PBS for flow cytometric analysis, with the control without wh-CQDs. Flow cytometry data were analyzed using CytExpert software.

## 3. Results and Discussion

### 3.1. Synthesis and Characterization of wh-CQDs

Wh is an outstanding precursor for synthetic carbon nanodots because it contains many secondary metabolites, such as phenols, flavonoids, sterols, terpenoids, and anthraquinones, which act as stabilizers and accelerators in the green synthesis of nanoparticles [40,41]. In wh-CQDs synthesis, the hydrolysis and decomposition of carbohydrates in wh through a bottom-up hydrothermal method leads to the loss of water, and the formed products react to form aromatic compounds during polymerization and condensation. Finally, a nuclear explosion occurs to form carbon quantum dots. Green synthesis enables the production of carbon and carbon hybrid materials with controllable structure and morphology in an energy-saving manner [42,43]. The synthetic route for the CQDs derived from wh is illustrated in Figure 1.

The morphology of the wh-CQDs was evaluated using TEM. As shown in Figure 2a, the as-prepared wh-CQDs were uniform in size and well-dispersed throughout the cross-section with high monodispersity. As shown in the inset of Figure 2a, the HRTEM image showed that the wh-CQDs exhibited an interplanar spacing of 0.21 nm, which confirmed the presence of graphitic carbon structures [44]. In addition, the corresponding particle size histograms of the wh-CQDs were obtained by selecting 100 nanoparticles for analysis using the ImageJ 1.52 software (Figure 2b). The statistical results showed that the particle size distribution of wh-CQDs ranged from 1.2 to 4.2 nm with an average diameter of  $2.44 \pm 0.57$  nm. The small particle size and high dispersibility of the synthesized wh-CQDs are attributable to the uniform energy and high pressure generated in the hydrothermal reaction.

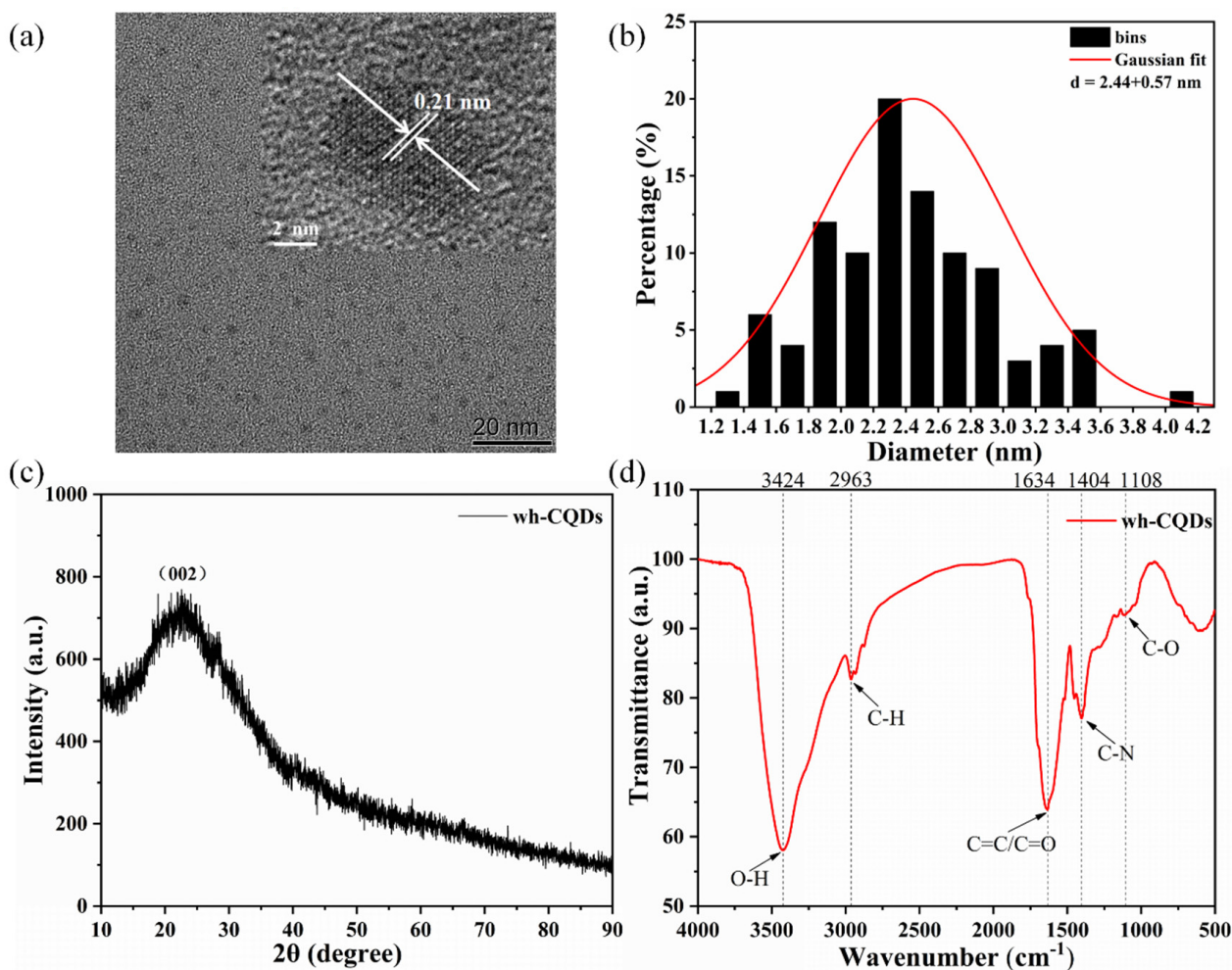


**Figure 2.** Characterization of wh-CQDs: (a) TEM image (inset: HRTEM image), (b) the size distribution of particles, (c) XRD pattern, (d) FTIR spectra.

Figure 2c shows the XRD patterns of the synthesized wh-CQDs recorded in the range of  $2\theta = 10\text{--}90^\circ$ . The XRD pattern of the wh-CQDs exhibits a broad peak at  $2\theta = 23^\circ$ , which was consistent with the standard XRD pattern of PDF #39-1889 card and could be assigned to the diffraction of the (002) lattice plane, confirming the disordered graphitic structure [45,46]. Therefore, the wh-CQDs were amorphous spherical nanoparticles based on the TEM and XRD results. Furthermore, the surface structure and functional groups of the wh-CQDs were characterized using FTIR spectroscopy (Figure 2d). The FTIR spectra showed different characteristic absorption peaks attributed to the stretching and bending vibrations of different groups (O–H, C–H, C=O, C=C, C–N, and C–O). The broad band at  $3424\text{ cm}^{-1}$  was attributed to the O–H stretching vibration, and the absorption band at  $2963\text{ cm}^{-1}$  was assigned to C–H stretching [47]. The absorption peaks at  $1634$ ,  $1404$ ,  $1108\text{ cm}^{-1}$  were assigned to the stretching vibrations of C=O/C=C, C–N, and C–O groups, respectively [48,49]. These functional groups demonstrate that the surface of wh-CQDs contained hydroxyl and carboxylic groups, which determine the hydrophilicity and stability of wh-CQDs in aqueous solutions.

To further determine the elemental composition of the wh-CQDs, the samples were characterized using XPS. As shown in Figure 3a, the XPS spectra of wh-CQDs obtained in the full wavelength range exhibit three typical strong peaks at 284.8, 399.8, and 531.6 eV, which were attributed to C1s, N1s, and O1s, respectively, indicating that the wh-CQDs contained C (70.91%), N (8.38%), and O (20.71%). The high-resolution C1s spectrum (Figure 3b) reveals three main deconvolution peaks at 284.7, 286.1, and 287.8 eV, corresponding to the

C–C/C=C, C–N/C–O, and C=O surface groups of the wh-CQDs [12]. Similarly, the three peaks in the N1s spectrum (Figure 3c) appeared at 399.8, 398.2, and 401.5 eV, representing C–N–C, C=N–C, and N–H, respectively [50,51]. In the O1s spectrum (Figure 3d), three main peaks with binding energies of 531.3, 532.6, and 533.8 eV were observed; they were assigned to C=O, C–OH/C–O–C, and –COOH, respectively [35]. In general, XPS analysis showed that the surface of wh-CQDs contained multiple O- with N- functional groups, which was consistent with the FTIR results and illustrated that wh-CQDs are highly water-soluble.

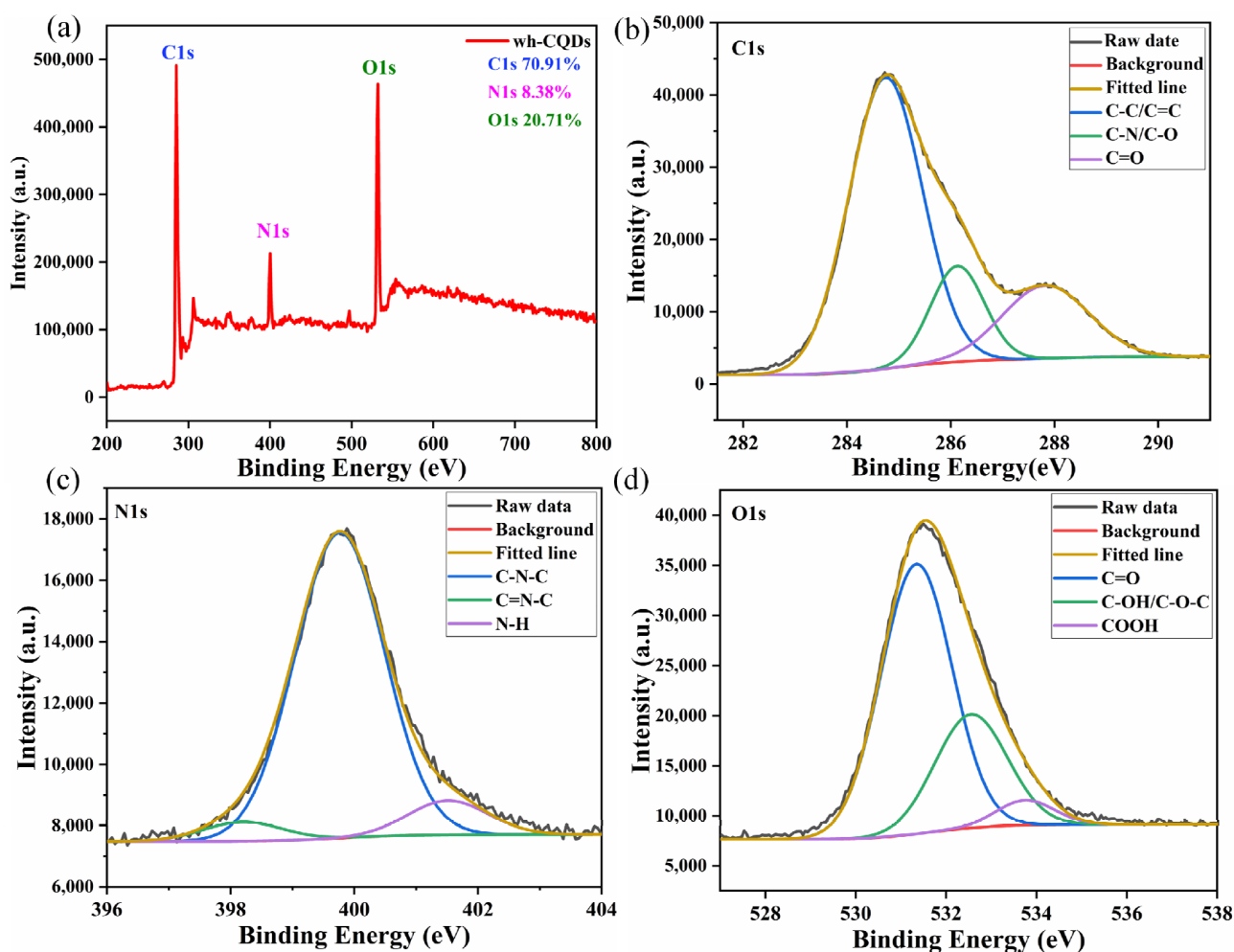


**Figure 3.** (a) XPS full-survey spectrum of wh-CQDs. The high-resolution deconvoluted XPS peaks of wh-CQDs for (b) C1s, (c) N1s, and (d) O1s.

### 3.2. Optical Properties of wh-CQDs

The optical characteristics of the wh-CQDs (100  $\mu\text{g}/\text{mL}$ ) were determined by measuring the UV-Vis absorption spectra, photoluminescence spectra and time-resolved fluorescence spectra. The diluted wh-CQDs exhibited good water solubility at room temperature. The aqueous wh-CQD solution was brown under daylight and bright blue under 365-nm UV light (inset, Figure 4a). Figure 4a shows the ultraviolet absorption and fluorescence spectra of the wh-CQDs. The wh powder has no absorption peak at 270 nm. Compared with the wh powder, the wh-CQDs exhibited a large absorption peak at 270 nm, which was attributed to the C=C/C=N  $\pi$ - $\pi^*$  transition of the  $\text{SP}^2$  hybrid domain. In the fluorescence spectra of wh-CQDs, the optimal excitation wavelength was 340 nm, and the optimal emission wavelength was 420 nm. As shown in Figure 4b, the fluorescence intensity of the wh-CQDs increased at excitation wavelengths of 320–340 nm and decreased at 340–400 nm. Wh-CQDs exhibited typical excitation-light-dependent emission characteristics. There are

two typical luminescence models for this property: bandgap transitions in the conjugated  $\pi$  domain and surface defects of CQDs. According to the former mechanism, some studies have attributed the luminescence redshift of CQDs to the quantum size effect [52,53]. In the latter mechanism, the surface state is the main factor affecting the fluorescence change [54,55]. In the present study, owing to the size composite Gaussian distribution of the wh-CQDs, the excitation light dependence may be caused by surface-state defects. Figure 4c shows the three-dimensional fluorescence spectra of the wh-CQDs with a large fluorescence circle at an excitation wavelength of 340 nm and an emission wavelength of 420 nm, corresponding to the fluorescence emission spectra of the wh-CQDs. Figure 4d shows the fluorescence decay profile for wh-CQDs at an excitation/emission wavelength of 340/420 nm, which is in line with biexponential fitting curve with an average lifetime of 2.2 ns. The QY of the wh-CQDs was calculated to be 3.3%, using quinine sulfate as the fluorescence standard reference (Figure 4e). As shown in Table S1, five different concentrations of wh-CQDs and quinine sulfate solutions were explained.

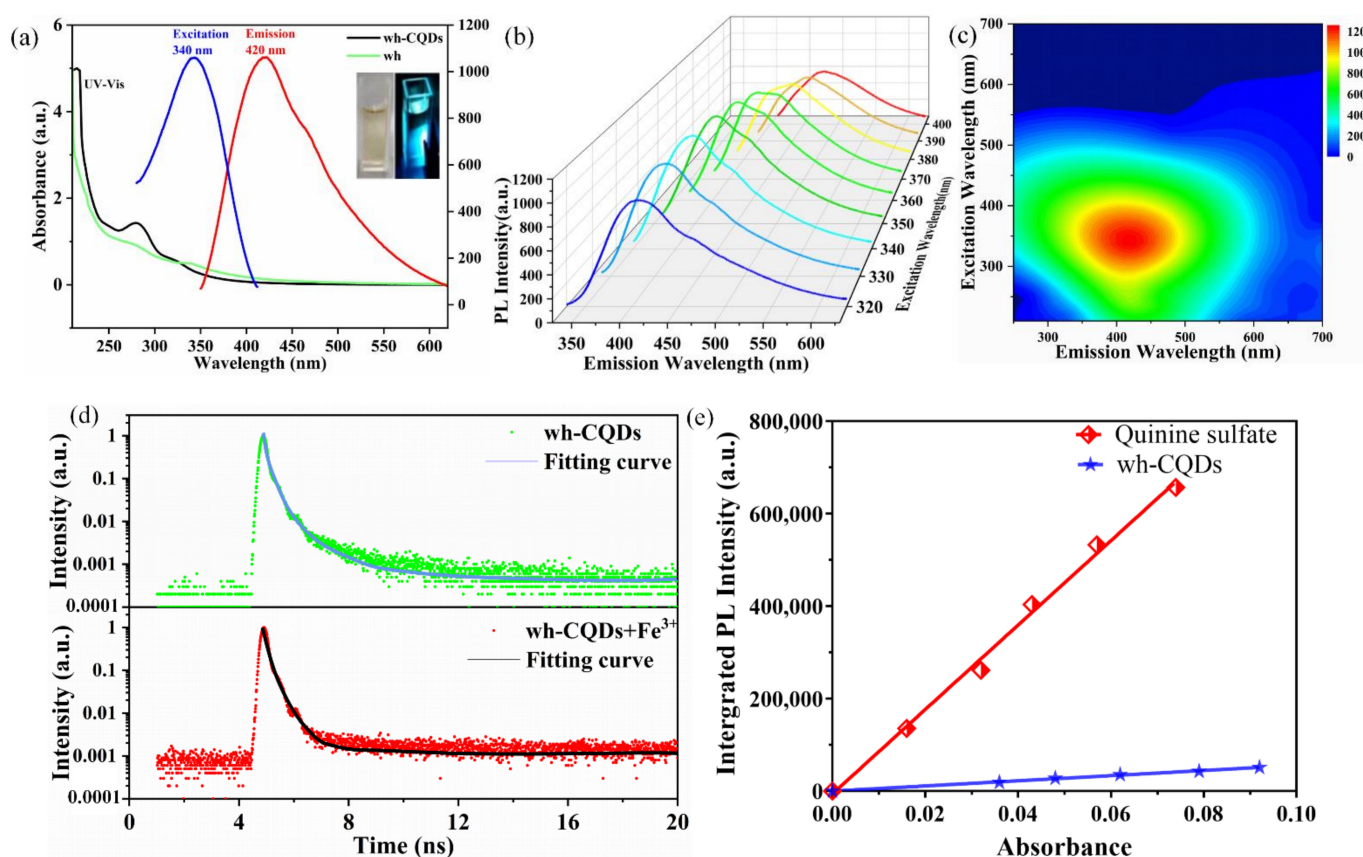


**Figure 4.** (a) UV-vis absorption with maximum fluorescence excitation and fluorescence emission spectra of the wh-CQDs, (b) Fluorescence emission spectra of the wh-CQDs at different excitation wavelengths ranging from 320 to 400 nm (increments of 10 nm), (c) 3D fluorescence contour map of the wh-CQDs, (d) Fluorescence decay curve of wh-CQDs before and after the addition of 100  $\mu\text{M}$  of  $\text{Fe}^{3+}$ , (e) QY measurement of wh-CQDs using quinine sulfate as the reference.

### 3.3. Stability of wh-CQDs

To determine the stability of the wh-CQDs in cell imaging and sensing, the effects of acidic/basic, salt ionic concentrations, and irradiation times on the fluorescence intensity was examined. As shown in Figure 5a, the fluorescence intensity of the wh-CQDs was highest at pH 8 and tended to be stable in weakly acidic and weakly alkaline pH environments. No apparent changes were observed in the fluorescence intensity of the wh-CQDs at NaCl concentrations of 0.02–0.2 M (Figure 5b). In addition, the fluorescence intensity of the wh-CQDs remained stable under uninterrupted UV irradiation (Figure 5c).

All experiments were based on the results of three parallel experiments. These results are consistent with those of previous studies [56,57]. The outstanding stability of wh-CQDs enables their further application in sensing and bioimaging.

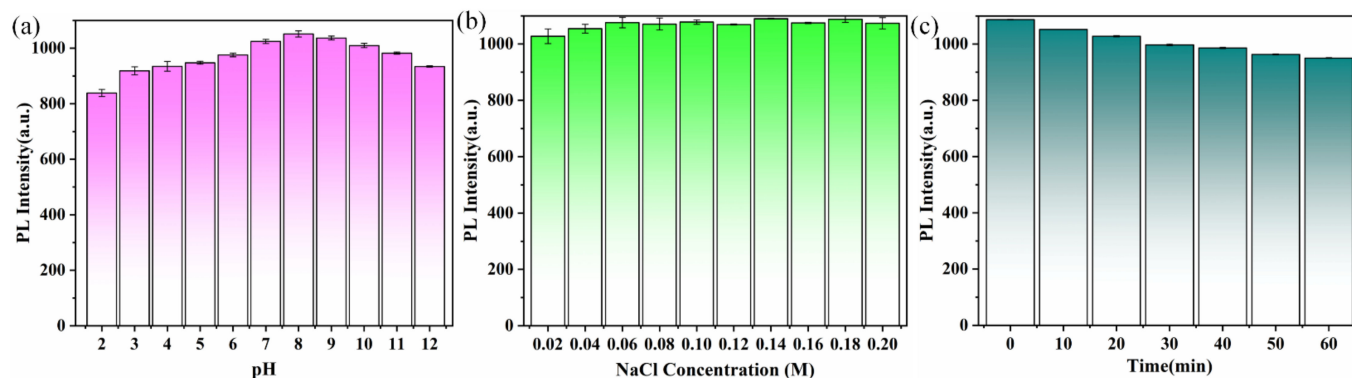


**Figure 5.** (a) Stability of fluorescence intensity of the wh-CQDs at different pH values, (b) NaCl concentrations, (c) exposure to UV light (0–60 min).

### 3.4. Fluorescent and Colorimetric Detection of $\text{Fe}^{3+}$

The applications of wh-CQDs in the environmental sciences and biology have been extensively investigated owing to their strong fluorescence properties and excellent stability. In this study, we used wh-CQDs as fluorescent probes to detect  $\text{Fe}^{3+}$ . The fluorescence intensity of the wh-CQDs was recorded at an excitation wavelength of 340 nm. The selectivity of wh-CQDs for  $\text{Fe}^{3+}$  was evaluated by adding metal ions in the presence and absence of  $\text{Fe}^{3+}$ , including  $\text{Fe}^{2+}$ ,  $\text{Mg}^{2+}$ ,  $\text{NH}_4^+$ ,  $\text{Ni}^{2+}$ ,  $\text{Zn}^{2+}$ ,  $\text{K}^+$ ,  $\text{Na}^+$ ,  $\text{Mn}^{2+}$ ,  $\text{Co}^{2+}$ ,  $\text{Ba}^{2+}$ ,  $\text{Al}^{3+}$ ,  $\text{Ca}^{2+}$ , and  $\text{Cu}^{2+}$  (Figure S1). As shown in Figure 6a,  $F$  and  $F_0$  are the fluorescence intensities at 340 nm in the presence and absence of the metal ions, respectively. Apparently, the fluorescence of wh-CQDs was quenched by 70% when  $\text{Fe}^{3+}$  was introduced, while in the presence of other metal ions the change was small ( $\text{Fe}^{2+}$ ,  $\text{Ni}^{2+}$ ,  $\text{Co}^{2+}$ , and  $\text{Cu}^{2+}$ ) or negligible ( $\text{Mg}^{2+}$ ,  $\text{NH}_4^+$ ,  $\text{Zn}^{2+}$ , and  $\text{Al}^{3+}$ ). At the same time, when  $\text{Fe}^{3+}$  was introduced into the wh-CQD solution in the presence of metal ions, the fluorescence intensity was still significantly quenched (red column). Therefore, the as-prepared wh-CQDs exhibited fascinating anti-interference ability with high selectivity for  $\text{Fe}^{3+}$  compared to other metal ions. The high selectivity of the wh-CQDs can be attributed to the chelation interactions between the N and O functional groups on the surface of the wh-CQDs and  $\text{Fe}^{3+}$ . Specifically, the electron-deficient  $\text{Fe}^{3+}$  maintained a half-filled 3d orbital to accept electrons, and the  $-\text{OH}$  and  $-\text{COOH}$  groups on the surface of the wh-CQDs after the introduction of  $\text{Fe}^{3+}$  rapidly reacted with  $\text{Fe}^{3+}$  to promote the transfer of excited electrons from the wh-CQDs to the 3d orbital of  $\text{Fe}^{3+}$ , resulting in non-radiative electron/hole recombination that quenched the fluorescence of the wh-CQDs [58–60]. The quenching mechanism of wh-CQDs induced by  $\text{Fe}^{3+}$  was investigated by measuring decay lifetimes. The decay lifetime would be a strong evidence to differentiate static quenching (decay lifetime hardly changed) and dynamic quenching (decay lifetime changed) [61–63]. The fluorescence lifetime of wh-CQDs is calculated as 2.2 ns in the absence of  $\text{Fe}^{3+}$ , and the change in fluorescence lifetime after the addition of  $\text{Fe}^{3+}$  was almost negligible as 1.9 ns (Figure 4d). Therefore, static quenching plays a major role in the fluorescence quenching of wh-CQDs.

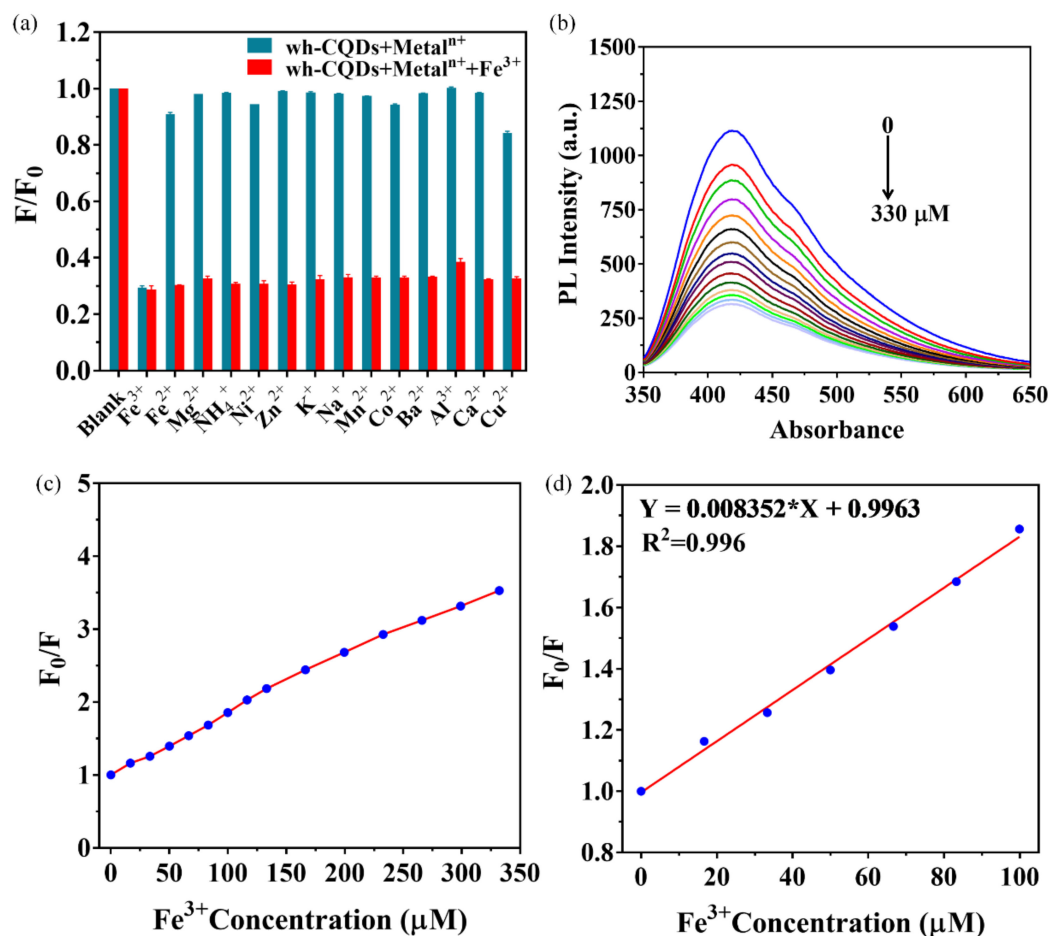


**Figure 6.** (a) The relative fluorescence intensities ( $F/F_0$ ) of the wh-CQDs in the presence of individual metal ions (blue column) and co-presence of  $Fe^{3+}$  ion with other metal ions (red column), (b) the fluorescent emission spectra of the wh-CQDs under various  $Fe^{3+}$  ion concentrations (0–330  $\mu M$ ), (c) the dependence of relative fluorescence ( $F/F_0$ ) of the wh-CQDs on the concentration of  $Fe^{3+}$  ions ranging from 0–330  $\mu M$ , (d) the Stern–Volmer plots for the concentration of  $Fe^{3+}$  in the range of 0–100  $\mu M$ .

For the sensitivity experiments, the fluorescence intensities at different concentrations of  $Fe^{3+}$  were investigated under 340-nm excitation light (Figure 6b). The fluorescence intensity of the wh-CQDs was sharply quenched by adding  $Fe^{3+}$  from 0 to 330  $\mu M$  (Figure 6c). The ratio of the initial fluorescence intensity to the fluorescence intensity ( $F_0/F$ ) at 340 nm excitation light was a linear function of the  $Fe^{3+}$  concentration in the range of 0–100  $\mu M$  with a correlation coefficient of 0.996, as shown in Figure 6d. The fluorescence quenching of the wh-CQDs follows the Stern–Volmer Equation (3).

$$\frac{F_0}{F} - 1 = K_{SV}[C] \quad (3)$$

where  $F_0$  and  $F$  are the emission intensities of the wh-CQDs at 340 nm in the absence and presence of  $Fe^{3+}$ , respectively;  $K_{SV}$  is the Stern–Volmer burst constant; and  $[C]$  is the  $Fe^{3+}$  concentration. The detection limit was calculated using the formula  $LOD = 3\sigma/S$ , where  $\sigma$  represents the standard deviation of the fluorescence intensity of the blank wh-CQDs, and  $S$  is the slope of the linear function ( $n = 10$ ). From the results obtained, we calculated the detection limit to be 0.084  $\mu M$ . Notably, the obtained detection limit of  $Fe^{3+}$  by the wh-CQDs was much lower than that proposed by the World Health Organization (5.36  $\mu M$ ), indicating that the wh-CQDs can be applied in highly selective sensing of  $Fe^{3+}$ . A comparison of different systems for  $Fe^{3+}$  determination is summarized in Table 1, indicating

that the detection limits of CQDs derived from biomass are comparable to or lower than those proposed earlier.

**Table 1.** Comparison of the Fe<sup>3+</sup> detection sensitivity between the wh-CQDs and other reported CQDs.

Sensing Platform	Carbon Source	Synthesis Method	Linear Range (μM)	LOD (μM)	R <sup>2</sup>	Ref.
Nitrogen-doped carbon dots	Poa pratensis	Carbonization	5–25	1.4	0.997	[47]
C-dots	Ananas erectifolius	Hydrothermal	0–30	0.77	0.997	[1]
CDs	Mint	Carbonization	0–400	0.037	0.995	[58]
S-doped carbon quantum	Ascorbic acid and thioglycolic	Hydrothermal	0–200	0.05	0.995	[59]
N-CDs	Diethylenetriamine	Hydrothermal	2–50	10.42	0.996	[60]
Wh-CQDs	Water hyacinth	Hydrothermal	0–330	0.084	0.996	This work

### 3.5. Cytotoxicity and Cell Imaging

CQDs are used as probes in various fields owing to their excellent tunable fluorescence properties, colorful fluorescence emission, small size, high photostability, and biocompatibility [64–66]. In the present study, to assess the cell viability of wh-derived biomass carbon spots, hydrogen-producing bacterium *Klebsiella* sp. was used as a model for toxicity studies. As shown in Figure 7, cell viability was unaffected by changes in the concentration of the wh-CQDs. At the wh-CQD concentration of 1000 μg/mL, cell viability was still above 90%. At low concentrations, the cell viability was largely unaltered, indicating that wh-CQDs possessed low toxicity toward the hydrogen-producing bacterium *Klebsiella* sp.

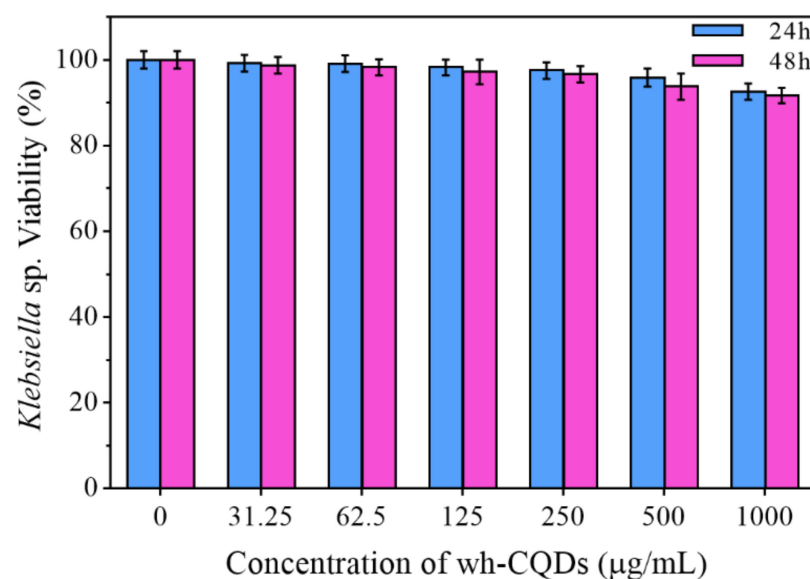


**Figure 7.** Cell viability assays of the *Klebsiella* sp. treated with different concentrations of wh-CQDs for 24 and 48 h.

As shown in Figure 8, imaging studies were performed after culturing the hydrogen-producing bacterium *Klebsiella* sp. in a medium containing 500 μg/mL wh-CQDs for 12 h. As observed using laser confocal microscopy, the CQDs exhibited an intense blue fluorescence signal at excitation wavelengths of 375–407 nm with outstanding imaging potential. Notably, *Klebsiella* sp. cell walls contain various polysaccharides and lipids, which make them difficult to be labeled. The wh-CQDs could enter the bacterial membrane via endocytosis, indicating that the wh-CQDs have strong penetrating ability. Therefore, owing to the strong fluorescence, stability, and good biocompatibility of wh-CQDs, they are expected to be an effective fluorescent probe for bacterial cell tracers in the bioenergy field.

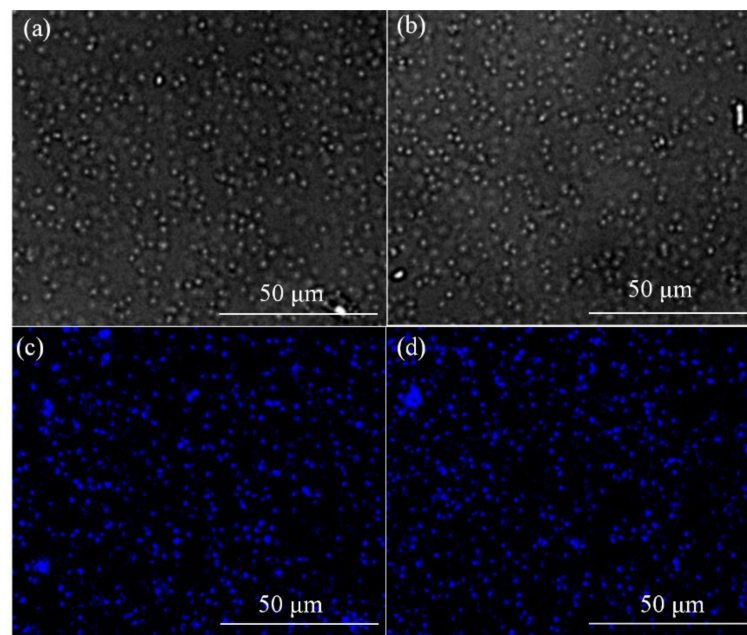


**Figure 8.** Fluorescence image of *Klebsiella* sp. cells incubated with wh-CQDs (500  $\mu\text{g}/\text{mL}$ ) for 12 h under (a–b) bright field and (c–d) excitation wavelength of 375–407 nm.

### 3.6. Flow Cytometry Analysis of Intracellular wh-CQDs

Based on the cellular imaging results, we determined the proportion of wh-CQD uptake by *Klebsiella* sp. cells. To this end, cells were incubated with 500  $\mu\text{g}/\text{mL}$  wh-CQDs and analyzed by flow cytometry after incubation for 12 and 24 h at 37  $^{\circ}\text{C}$ . The emission of wh-CQDs was analyzed in the FITC fluorescence channel. As shown in Figure 9a, the relative fluorescence intensity of  $10^5$  CFU/mL of unstained *Klebsiella* sp. was extremely weak, and the fluorescence was mainly biological autofluorescence. As shown in Figure 9b, the relative fluorescence intensity of *Klebsiella* sp. labeled with wh-CQDs in the P2 region was significantly enhanced, which could be distinguished from the unstained cell clusters. The P2 region incubated for 12 h accounted for 32.89% of the total cell number, indicating that the proportion of wh-CQDs-labeled *Klebsiella* sp. accounted for 32.89% of the total cell number. Similarly, in Figure 9c, the proportion of labeling accounted for 41.78% of the total cell number incubated for 24 h. Therefore, these data highlight a different time course and proportion of internalization of wh-CQDs in *Klebsiella* sp. cells.

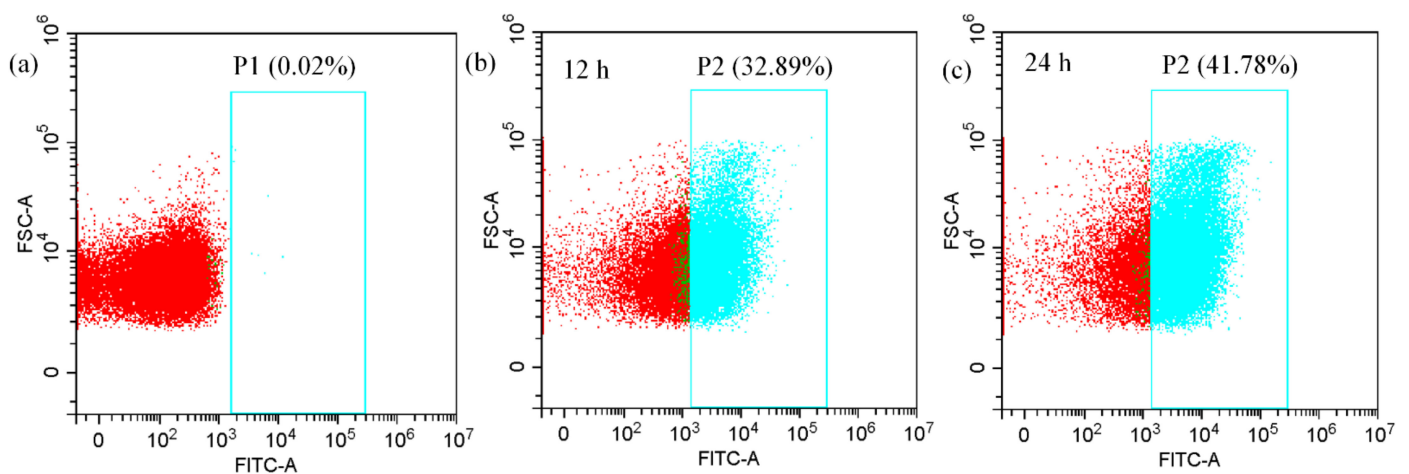


**Figure 9.** Proportion of wh-CQDs internalized in *Klebsiella* sp. by flow cytometry analyses. (a) without wh-CQDs, (b) *Klebsiella* sp. cells incubated with wh-CQDs (500  $\text{mg}/\text{mL}$ ) for 12 h and (c) 24 h.

#### 4. Conclusions

In the present study, blue fluorescent CQDs were derived from natural biomass wh using a bottom-up hydrothermal method at 180 °C for 12 h. The synthesized wh-CQDs were uniform in size, with an average size of  $2.44 \pm 0.57$  nm, and exhibited typical excitation-light-dependent properties owing to surface state defects. The wh-CQDs exhibited excellent physicochemical properties with high selectivity and sensitivity to  $\text{Fe}^{3+}$ . In addition, toxicity and imaging studies on the hydrogen-producing bacterium *Klebsiella* sp. and flow cytometry analysis of intracellular wh-CQDs were performed for the first time using biomass-derived carbon dots. Owing to the green synthesis of wh-CQDs, even at high concentrations (1000  $\mu\text{g}/\text{mL}$ ), wh-CQDs showed low cytotoxicity toward hydrogen-producing bacteria. Notably, the synthesized wh-CQDs possessed strong penetrating ability and good biocompatibility, and were able to break through the lipid and polysaccharide barrier in *Klebsiella* sp. cell wall. The wh-CQDs entered bacterial cells and emitted bright blue fluorescence, implying that they may be an effective probe for flow cytometry. However, the long-term performance of wh-CQDs tracer analysis in *Klebsiella* sp. is still lacking, and the analysis of bacterial cell imaging mechanism is not deep enough, which needs to be further improved in the future research work. Overall, our study expands the application of biomass carbon spots and demonstrates that wh carbon spots can be used as sensitive fluorescent probes for  $\text{Fe}^{3+}$  detection and cellular imaging.

**Supplementary Materials:** The following are available online at <https://www.mdpi.com/article/10.3390/nano12091528/s1>, Table S1. Wh-CQDs and Quinine Sulfate Concentration for Measuring QY; Figure S1. Selectivity of the wh-CQDs toward different metal ions.

**Author Contributions:** Conceptualization, P.Z. and Q.Z.; methodology, J.C., Y.L., C.Q. and J.Y.; data curation, P.Z., J.C., S.X. and Y.Z.; investigation, P.Z., Q.Z. and Y.L.; writing—original draft preparation, P.Z.; writing—review and editing, Q.Z., Y.L. and P.Z.; supervision, Q.Z. and Y.L.; funding acquisition, Q.Z. and Y.L. All authors have read and agreed to the published version of the manuscript.

**Funding:** This work was financially supported by the National Natural Science Foundation of China (21406150); the National Natural Science Foundation of Anhui Province (2108085MB34); the Key Research and Development Project of Anhui Province in China (201904a07020003); the Top Young and Middle-aged Talents Program of Anhui Polytechnic University in China (S022019014); the Practice and Innovation Project of Postgraduate of Anhui Polytechnic University in China (Y412021014).

**Institutional Review Board Statement:** Not applicable.

**Informed Consent Statement:** Not applicable.

**Data Availability Statement:** The data will made available on request.

**Conflicts of Interest:** The authors declare no conflict of interest.

#### References

1. Raja, S.; Buhl, E.M.; Dreschers, S.; Schalla, C.; Zenke, M.; Sechi, A.; Mattoso, L.H.C. Curaua-derived carbon dots: Fluorescent probes for effective Fe(III) ion detection, cellular labeling and bioimaging. *Mater. Sci. Eng. C Mater. Biol. Appl.* **2021**, *129*, 112409. [[CrossRef](#)] [[PubMed](#)]
2. Wang, Y.; Sun, J.; He, B.; Feng, M. Synthesis and modification of biomass derived carbon dots in ionic liquids and their application: A mini review. *GreenChE* **2020**, *1*, 15. [[CrossRef](#)]
3. Rawat, S.; Mishra, R.K.; Bhaskar, T. Biomass derived functional carbon materials for supercapacitor applications. *Chemosphere* **2022**, *286*, 131961. [[CrossRef](#)] [[PubMed](#)]
4. He, Z.Y.; Li, Y.X.; Liu, C.; Li, Y.; Qian, M.M.; Zhu, Y.C.; Wang, X.F. Controllable conversion of biomass to lignin-silica hybrid nanoparticles: High-performance renewable dual-phase fillers. *Waste Manag.* **2021**, *135*, 381–388. [[CrossRef](#)]
5. Rajamohan, N.; Al Shibli, F.S.Z.S. Synthesis and application of carbon substrate nano material from biomass for surface protection - Effect of variables, electrochemical and isotherm studies. *Chemosphere* **2022**, *292*, 133479. [[CrossRef](#)]
6. Feng, Y.; Liu, L.; Liu, X.Y.; Li, Y.X.; Wu, Y.P.; Zhu, Y.C.; Wang, X.F. N-Enriched Porous Carbon/SiO<sub>2</sub> Composites Derived from Biomass Rice Husks for Boosting Li-Ion Storage: Insight into the Effect of N-Doping. *Chemistry* **2021**, *27*, 10749–10757. [[CrossRef](#)]

7. Li, X.; Zhang, S.X.; Zhang, M.M.; Yu, M.W.; Chen, H.; Yang, H.W.; Xu, Q. One-step synthesis of mixed valence FeO<sub>x</sub> nanoparticles supported on biomass activated carbon for degradation of bisphenol A by activating peroxydisulfate. *J. Hazard Mater.* **2021**, *409*, 124990. [[CrossRef](#)]
8. Li, D.; Yang, T.X.; Liu, Z.G.; Xia, Y.; Chen, Z.L.; Yang, S.S.; Gai, C.; Bhatnagar, A.; Ng, Y.H.; Ok, Y.S. Green synthesis of graphite-based photo-Fenton nanocatalyst from waste tar via a self-reduction and solvent-free strategy. *Sci. Total Environ.* **2022**, *824*, 153772. [[CrossRef](#)]
9. Zha, Y.C.; Xin, R.J.; Zhang, M.Y.; Cui, X.; Li, N. Stimuli-responsive azobenzene-quantum dots for multi-sensing of dithionite, hypochlorite, and azoreductase. *Mikrochim. Acta* **2020**, *187*, 481. [[CrossRef](#)]
10. Probst, C.E.; Zrazhevskiy, P.; Bagalkot, V.; Gao, X. Quantum dots as a platform for nanoparticle drug delivery vehicle design. *Adv. Drug Deliv. Rev.* **2013**, *65*, 703–718. [[CrossRef](#)]
11. Min, H.; Qi, Y.Q.; Chen, Y.H.; Zhang, Y.L.; Han, X.X.; Xu, Y.; Liu, Y.; Hu, J.S.; Liu, H.B.; Li, Y.Y.; et al. Synthesis and Imaging of Biocompatible Graphdiyne Quantum Dots. *ACS Appl. Mater. Interfaces* **2019**, *11*, 32798–32807. [[CrossRef](#)] [[PubMed](#)]
12. Liang, Y.M.; Yang, H.; Zhou, B.; Chen, Y.; Yang, M.; Wei, K.S.; Yan, X.F.; Kang, C. Waste tobacco leaves derived carbon dots for tetracycline detection: Improving quantitative accuracy with the aid of chemometric model. *Anal. Chim. Acta* **2022**, *1191*, 339269. [[CrossRef](#)] [[PubMed](#)]
13. Bai, Y.; Wang, Y.; Cao, L.P.; Jiang, Y.J.; Li, Y.F.; Zou, H.Y.; Zhan, L.; Huang, C.Z. Self-Targeting Carbon Quantum Dots for Peroxynitrite Detection and Imaging in Live Cells. *Anal. Chem.* **2021**, *93*, 16466–16473. [[CrossRef](#)]
14. Chen, Y.N.; Cheng, H.X.; Wang, W.N.; Jin, Z.; Liu, Q.; Yang, H.Y.; Cao, Y.; Li, W.D.; Fakhri, A.; Gupta, V.K. Preparation of carbon dots-hematite quantum dots-loaded hydroxypropyl cellulose-chitosan nanocomposites for drug delivery, sunlight catalytic and antimicrobial application. *J. Photochem. Photobiol. B* **2021**, *219*, 112201. [[CrossRef](#)] [[PubMed](#)]
15. He, X.; Luo, Q.; Zhang, J.; Chen, P.; Wang, H.J.; Luo, K.; Yu, X.Q. Gadolinium-doped carbon dots as nano-theranostic agents for MR/FL diagnosis and gene delivery. *Nanoscale* **2019**, *11*, 12973–12982. [[CrossRef](#)]
16. Qureashi, A.; Pandith, A.H.; Bashir, A.; Malik, L.A. Biomass-derived carbon quantum dots: A novel and sustainable fluorescent “ON-OFF-ON” sensor for ferric ions. *Anal. Methods* **2021**, *13*, 4756–4766. [[CrossRef](#)]
17. Wang, Z.Q.; Cheng, F.C.; Cai, H.C.; Li, X.R.; Sun, J.P.; Wu, Y.Q.; Wang, N.N.; Zhu, Y.Q. Robust versatile nanocellulose/polyvinyl alcohol/carbon dot hydrogels for biomechanical sensing. *Carbohydr. Polym.* **2021**, *259*, 117753. [[CrossRef](#)]
18. Zairov, R.R.; Dovzhenko, A.P.; Sarkanich, K.A.; Nizameev, I.R.; Luzhetskiy, A.V.; Sudakova, S.N.; Podyachev, S.N.; Burilov, V.A.; Vatsouro, I.M.; Vomiero, A.; et al. Single Excited Dual Band Luminescent Hybrid Carbon Dots-Terbium Chelate Nanothermometer. *Nanomaterial* **2021**, *11*, 3080. [[CrossRef](#)]
19. Zhu, S.J.; Song, Y.B.; Wang, J.; Wan, H.; Zhang, Y.; Ning, Y.; Yang, B. Photoluminescence mechanism in graphene quantum dots: Quantum confinement effect and surface/edge state. *Nano Today* **2016**, *13*, 10–14. [[CrossRef](#)]
20. Chatzimitakos, T.; Kasouni, A.; Sygellou, L.; Leonardos, I.; Troganis, A.; Stalikas, C. Human fingernails as an intriguing precursor for the synthesis of nitrogen and sulfur-doped carbon dots with strong fluorescent properties: Analytical and bioimaging applications. *Sens. Actuators B Chem.* **2018**, *267*, 494–501. [[CrossRef](#)]
21. Zhou, C.; Wu, S.W.; Qi, S.H.; Song, W.J.; Sun, C.Y. Facile and High-yield Synthesis of N-doped Carbon Quantum Dots from Biomass Quinoa Saponin for the Detection of Co<sup>2+</sup>. *J. Anal. Methods Chem.* **2021**, *2021*, 9732364. [[CrossRef](#)] [[PubMed](#)]
22. Chauhan, P.; Mundekkad, D.; Mukherjee, A.; Chaudhary, S.; Umar, A.; Baskoutas, S. Coconut Carbon Dots: Progressive Large-Scale Synthesis, Detailed Biological Activities and Smart Sensing Aptitudes towards Tyrosine. *Nanomaterials* **2022**, *12*, 162. [[CrossRef](#)] [[PubMed](#)]
23. Meng, W.X.; Wang, B.Y.; Ai, L.; Song, H.Q.; Lu, S.Y. Engineering white light-emitting diodes with high color rendering index from biomass carbonized polymer dots. *J. Colloid Interface Sci.* **2021**, *598*, 274–282. [[CrossRef](#)] [[PubMed](#)]
24. Jagannathan, M.; Dhinasekaran, D.; Soundharraj, P.; Rajendran, S.; Vo, D.N.; Prakasarao, A.; Ganesan, S. Green synthesis of white light emitting carbon quantum dots: Fabrication of white fluorescent film and optical sensor applications. *J. Hazard Mater.* **2021**, *416*, 125091. [[CrossRef](#)] [[PubMed](#)]
25. Tong, X.; Zhu, Y.F.; Tong, C.Y.; Shi, S.Y.; Long, R.Q.; Guo, Y. Simultaneous sensing gamma-glutamyl transpeptidase and alkaline phosphatase by robust dual-emission carbon dots. *Anal. Chim. Acta* **2021**, *1178*, 338829. [[CrossRef](#)]
26. Sun, X.; Jiang, M.W.; Chen, L.G.; Niu, N. Construction of ratiometric fluorescence MIPs probe for selective detection of tetracycline based on passion fruit peel carbon dots and europium. *Mikrochim. Acta* **2021**, *188*, 297. [[CrossRef](#)]
27. Wang, D.; Zhang, Y.; Cai, Z.; You, S.J.; Sun, Y.B.; Dai, Y.; Wang, R.Y.; Shao, S.L.; Zou, J.L. Corn Stalk-Derived Carbon Quantum Dots with Abundant Amino Groups as a Selective-Layer Modifier for Enhancing Chlorine Resistance of Membranes. *ACS Appl. Mater. Interfaces* **2021**, *13*, 22621–22634. [[CrossRef](#)]
28. Chan, M.H.; Chen, B.G.; Ngo, L.T.; Huang, W.T.; Li, C.H.; Liu, R.S.; Hsiao, M. Natural Carbon Nanodots: Toxicity Assessment and Theranostic Biological Application. *Pharmaceutics* **2021**, *13*, 1874. [[CrossRef](#)]
29. Liang, C.Z.; Xie, X.B.; Zhang, D.D.; Feng, J.; Lu, S.Y.; Shi, Q.S. Biomass carbon dots derived from *Wedelia trilobata* for the direct detection of glutathione and their imaging application in living cells. *J. Mater. Chem. B* **2021**, *9*, 5670–5681. [[CrossRef](#)]
30. Zhou, J.D.; Ge, M.; Han, Y.Q.; Ni, J.X.; Huang, X.; Han, S.Y.; Peng, Z.B.; Li, Y.D.; Li, S.J. Preparation of Biomass-Based Carbon Dots with Aggregation Luminescence Enhancement from Hydrogenated Rosin for Biological Imaging and Detection of Fe<sup>3+</sup>. *ACS Omega* **2020**, *5*, 11842–11848. [[CrossRef](#)]

31. Shen, J.; Shang, S.M.; Chen, X.Y.; Wang, D.; Cai, Y. Facile synthesis of fluorescence carbon dots from sweet potato for Fe<sup>3+</sup> sensing and cell imaging. *Mater. Sci. Eng. C Mater. Biol. Appl.* **2017**, *76*, 856–864. [[CrossRef](#)]
32. Sharma, N.; Das, G.S.; Yun, K. Green synthesis of multipurpose carbon quantum dots from red cabbage and estimation of their antioxidant potential and bio-labeling activity. *Appl. Microbiol. Biotechnol.* **2020**, *104*, 7187–7200. [[CrossRef](#)] [[PubMed](#)]
33. Wang, R.B.; Jiao, L.; Zhou, X.L.; Guo, Z.Y.; Bian, H.Y.; Dai, H.Q. Highly fluorescent graphene quantum dots from biorefinery waste for tri-channel sensitive detection of Fe<sup>3+</sup> ions. *J. Hazard Mater.* **2021**, *412*, 125096. [[CrossRef](#)] [[PubMed](#)]
34. Safranko, S.; Stankovic, A.; Hajra, S.; Kim, H.J.; Strelec, I.; Dutour-Sikiric, M.; Weber, I.; Bosnar, M.H.; Grbcic, P.; Pavelic, S.K.; et al. Preparation of Multifunctional N-Doped Carbon Quantum Dots from Citrus clementina Peel: Investigating Targeted Pharmacological Activities and the Potential Application for Fe<sup>3+</sup> Sensing. *Pharmaceuticals* **2021**, *14*, 857. [[CrossRef](#)] [[PubMed](#)]
35. Architha, N.; Ragupathi, M.; Shobana, C.; Selvankumar, T.; Kumar, P.; Lee, Y.S.; Kalai Selvan, R. Microwave-assisted green synthesis of fluorescent carbon quantum dots from Mexican Mint extract for Fe(3+) detection and bio-imaging applications. *Environ. Res.* **2021**, *199*, 111263. [[CrossRef](#)]
36. Chen, X.; Zhu, J.; Song, W.; Xiao, L.P. Integrated Cascade Biorefinery Processes to Transform Woody Biomass Into Phenolic Monomers and Carbon Quantum Dots. *Front. Bioeng. Biotechnol.* **2021**, *9*, 803138. [[CrossRef](#)]
37. Paul, A.; Kurian, M. N-doped photoluminescent carbon dots from water hyacinth for tumour detection. *Mater. Today Proc.* **2020**, *25*, 213–217. [[CrossRef](#)]
38. Gong, N.Q.; Wang, H.; Li, S.; Deng, Y.L.; Chen, X.A.; Ye, L.; Gu, W. Microwave-Assisted Polyol Synthesis of Gadolinium-Doped Green Luminescent Carbon Dots as a Bimodal Nanoprobe. *Langmuir* **2014**, *30*, 10933–10939. [[CrossRef](#)]
39. Li, C.J.; Wang, Y.Q.; Zhang, X.J.; Guo, X.L.; Kang, X.X.; Du, L.B.; Liu, Y. Red fluorescent carbon dots with phenylboronic acid tags for quick detection of Fe(III) in PC<sub>12</sub> cells. *J. Colloid Interface Sci.* **2018**, *526*, 487–496. [[CrossRef](#)]
40. Baccile, N.; Laurent, G.; Babonneau, F.; Fayon, F.; Titirici, M.M.; Antonietti, M. Structural Characterization of Hydrothermal Carbon Spheres by Advanced Solid-State MAS <sup>13</sup>C NMR Investigations. *J. Phys. Chem. C* **2009**, *113*, 9644–9654. [[CrossRef](#)]
41. Falco, C.; Perez Caballero, F.; Babonneau, F.; Gervais, C.; Laurent, G.; Titirici, M.M.; Baccile, N. Hydrothermal carbon from biomass: Structural differences between hydrothermal and pyrolyzed carbons via <sup>13</sup>C solid state NMR. *Langmuir* **2011**, *27*, 14460–14471. [[CrossRef](#)] [[PubMed](#)]
42. Jagathesan, G.; Rajiv, P. Biosynthesis and characterization of iron oxide nanoparticles using Eichhornia crassipes leaf extract and assessing their antibacterial activity. *Biocatal. Agric. Biotechnol.* **2017**, *13*, 90–94. [[CrossRef](#)]
43. Zhang, Q.; Xu, S.Y.; Li, Y.B.; Ding, P.F.; Zhang, Y.G.; Zhao, P. Green-synthesized nickel oxide nanoparticles enhances biohydrogen production of Klebsiella sp. WL1316 using lignocellulosic hydrolysate and its regulatory mechanism. *Fuel* **2021**, *305*, 121585. [[CrossRef](#)]
44. Tian, T.; Zhong, Y.P.; Deng, C.; Wang, H.; He, Y.; Ge, Y.L.; Song, G.W. Brightly near-infrared to blue emission tunable silver-carbon dot nanohybrid for sensing of ascorbic acid and construction of logic gate. *Talanta* **2017**, *162*, 135–142. [[CrossRef](#)] [[PubMed](#)]
45. Diao, H.P.; Li, T.T.; Zhang, R.; Kang, Y.; Liu, W.; Cui, Y.H.; Wei, S.Y.; Wang, N.; Li, L.; Wang, H.J.; et al. Facile and green synthesis of fluorescent carbon dots with tunable emission for sensors and cells imaging. *Spectrochim. Acta A Mol. Biomol. Spectrosc.* **2018**, *200*, 226–234. [[CrossRef](#)]
46. Krishnaiah, P.; Atchudan, R.; Perumal, S.; Salama, E.S.; Lee, Y.R.; Jeon, B.H. Utilization of waste biomass of Poa pratensis for green synthesis of n-doped carbon dots and its application in detection of Mn<sup>2+</sup> and Fe<sup>3+</sup>. *Chemosphere* **2022**, *286*, 131764. [[CrossRef](#)]
47. Bu, Y.M.; Yu, L.; Su, P.C.; Wang, L.X.; Sun, Z.L.; Sun, M.T.; Wang, X.K.; Huang, D.J.; Wang, S.H. Green-emitting carbon quantum dots as a dual-mode fluorescent and colorimetric sensor for hypochlorite. *Anal. Bioanal. Chem.* **2022**, *414*, 2651–2660. [[CrossRef](#)]
48. Wang, Y.; Chen, J.; Tian, J.K.; Wang, G.C.; Luo, W.K.; Huang, Z.B.; Huang, Y.; Li, N.; Guo, M.M.; Fan, X.G. Tryptophan-sorbitol based carbon quantum dots for theranostics against hepatocellular carcinoma. *J. Nanobiotechnology* **2022**, *20*, 78. [[CrossRef](#)]
49. Feng, X.W.; Han, G.D.; Cai, J.H.; Wang, X.Y. Au@Carbon quantum Dots-MXene nanocomposite as an electrochemical sensor for sensitive detection of nitrite. *J. Colloid Interface Sci.* **2022**, *607*, 1313–1322. [[CrossRef](#)]
50. Wang, X.; Yang, P.; Feng, Q.; Meng, T.T.; Wei, J.; Xu, C.Y.; Han, J.Q. Green Preparation of Fluorescent Carbon Quantum Dots from Cyanobacteria for Biological Imaging. *Polymers* **2019**, *11*, 616. [[CrossRef](#)]
51. Chellasamy, G.; Arumugasamy, S.K.; Govindaraju, S.; Yun, K. Green synthesized carbon quantum dots from maple tree leaves for biosensing of Cesium and electrocatalytic oxidation of glycerol. *Chemosphere* **2022**, *287*, 131915. [[CrossRef](#)] [[PubMed](#)]
52. Jiang, K.; Sun, S.; Zhang, L.; Lu, Y.; Wu, A.G.; Cai, C.Z.; Lin, H.W. Red, green, and blue luminescence by carbon dots: Full-color emission tuning and multicolor cellular imaging. *Angew. Chem. Int. Ed. Engl.* **2015**, *54*, 5360–5363. [[CrossRef](#)] [[PubMed](#)]
53. Gu, D.; Hong, L.; Zhang, L.; Liu, H.; Shang, S.M. Nitrogen and sulfur co-doped highly luminescent carbon dots for sensitive detection of Cd (II) ions and living cell imaging applications. *J. Photochem. Photobiol. B* **2018**, *186*, 144–151. [[CrossRef](#)] [[PubMed](#)]
54. Ding, H.; Yu, S.B.; Wei, J.S.; Xiong, H.M. Full-Color Light-Emitting Carbon Dots with a Surface-State-Controlled Luminescence Mechanism. *ACS Nano* **2016**, *10*, 484–491. [[CrossRef](#)]
55. Bharathi, D.; Siddlingeshwar, B.; Krishna, R.H.; Singh, V.; Kottam, N.; Divakar, D.D.; Alkheraif, A.A. Green and Cost Effective Synthesis of Fluorescent Carbon Quantum Dots for Dopamine Detection. *J. Fluoresc.* **2018**, *28*, 573–579. [[CrossRef](#)]
56. Magdy, G.; Abdel Hakiem, A.F.; Belal, F.; Abdel-Megied, A.M. Green one-pot synthesis of nitrogen and sulfur co-doped carbon quantum dots as new fluorescent nanosensors for determination of salinomycin and maduramicin in food samples. *Food Chem.* **2021**, *343*, 128539. [[CrossRef](#)]

57. Zhu, J.T.; Chu, H.Y.; Shen, J.W.; Wang, C.Z.; Wei, Y.M. Nitrogen and fluorine co-doped green fluorescence carbon dots as a label-free probe for determination of cytochrome c in serum and temperature sensing. *J. Colloid Interface Sci.* **2021**, *586*, 683–691. [[CrossRef](#)]
58. Chang, D.; Zhao, Z.H.; Shi, L.H.; Liu, W.L.; Yang, Y.X. Lysosome-targeted carbon dots for colorimetric and fluorescent dual mode detection of iron ion, in vitro and in vivo imaging. *Talanta* **2021**, *232*, 122423. [[CrossRef](#)]
59. Du, F.Y.; Cheng, Z.F.; Tan, W.; Sun, L.S.; Ruan, G.H. Development of sulfur doped carbon quantum dots for highly selective and sensitive fluorescent detection of Fe<sup>2+</sup> and Fe<sup>3+</sup> ions in oral ferrous gluconate samples. *Spectrochim. Acta A* **2020**, *226*, 117602. [[CrossRef](#)]
60. Yi, Z.H.; Li, X.M.; Zhang, H.Y.; Ji, X.L.; Sun, W.; Yu, Y.X.; Liu, Y.A.; Huang, J.X.; Sarshar, Z.; Sain, M. High quantum yield photoluminescent N-doped carbon dots for switch sensing and imaging. *Talanta* **2021**, *222*, 121663. [[CrossRef](#)]
61. Du, J.Y.; Yang, Y.; Shao, T.L.; Qi, S.Q.; Zhang, P.; Zhuo, S.J.; Zhu, C.Q. Yellow emission carbon dots for highly selective and sensitive OFF-ON sensing of ferric and pyrophosphate ions in living cells. *J. Colloid Interface Sci.* **2011**, *587*, 376–384. [[CrossRef](#)]
62. He, Y.Y.; Wang, Y.B.; Mao, G.N.; Liang, C.Y.; Fan, M. Ratiometric fluorescent nanoprobe based on carbon dots and multicolor CdTe quantum dots for multiplexed determination of heavy metal ions. *Anal. Chim. Acta* **2022**, *1191*, 339251. [[CrossRef](#)] [[PubMed](#)]
63. Pang, S.; Liu, S.Y. Dual-emission carbon dots for ratiometric detection of Fe<sup>3+</sup> ions and acid phosphatase. *Anal. Chim. Acta* **2020**, *1105*, 155–161. [[CrossRef](#)] [[PubMed](#)]
64. Xu, X.K.; Mo, L.Q.; Li, Y.D.; Pan, X.Q.; Hu, G.Q.; Lei, B.F.; Zhang, X.J.; Zheng, M.T.; Zhuang, J.L.; Liu, Y.L.; et al. Construction of Carbon Dots with Color-Tunable Aggregation-Induced Emission by Nitrogen-Induced Intramolecular Charge Transfer. *Adv. Mater.* **2021**, *33*, 2104872. [[CrossRef](#)] [[PubMed](#)]
65. Nguyen, H.A.; Srivastava, I.; Pan, D.P.J.; Gruebele, M. Unraveling the Fluorescence Mechanism of Carbon Dots with Sub-Single-Particle Resolution. *Acs Nano* **2020**, *14*, 6127–6137. [[CrossRef](#)] [[PubMed](#)]
66. Geng, X.; Sun, Y.Q.; Li, Z.H.; Yang, R.; Zhao, Y.M.; Guo, Y.F.; Xu, J.J.; Li, F.T.; Wang, Y.; Lu, S.Y.; et al. Retrosynthesis of Tunable Fluorescent Carbon Dots for Precise Long-Term Mitochondrial Tracking. *Small* **2019**, *15*, 1901517. [[CrossRef](#)]